Investigating the inequality of phase change coefficients using ISS experimental data

Unmeelan Chakrabarti[a], Jeffrey S Allen[b], Kishan Bellur[a,b,c]

[a] *Department of Mechanical and Materials Engineering, University of Cincinnati, Cincinnati, Ohio*
[b] *Department of Mechanical & Aerospace Engineering, Michigan Technological University, Houghton, Michigan*
[c] *Corresponding author, email:bellurkn@ucmail.uc.edu*

Abstract

Kinetic theory is a popular approach to model liquid-vapor phase change but accurate determination of evaporation and condensation coefficients remains a challenge. Reported values of coefficients vary by several orders of magnitude. For simplicity and convenience evaporation and condensation coefficients are assumed to be equal though there is little physical evidence to support this. This study presents a novel methodology to test this assumption using data from Constrained Vapor Bubble (CVB) experiments conducted on the International Space Station (ISS). The experiments consist of a quartz cuvette that is partially filled with n-pentane; heated and cooled at opposite ends to induce simultaneous evaporation and condensation around a central bubble. Data obtained from the NASA Physical Sciences Informatics (PSI) database enabled a three-dimensional reconstruction of the liquid-vapor interface. The net mass flux over the vapor bubble surface is zero at steady operation, providing a closure relationship for simultaneous and independent calculation of both evaporation and condensation coefficients. The resulting coefficient values are within 1% of each other, but are not equal. The two coefficients are also within 2% of those predicted using transition state theory. When the evaporation and condensation coefficients are forced to be equal, the deviation from transition state theory is approximately 60%. This deviation monotonically increases with increasing rates of evaporation/condensation due to a systemic under-prediction of the bubble surface area. The agreement between derived coefficients and those predicted by transition state theory is maintained when the bubble surface area is corrected to account for Marangoni-induced interfacial instabilities.

Keywords: evaporation, condensation, phase change, kinetic theory, accommodation coefficients, CVB, ISS

Nomenclature

Symbol	Description	Units
List of Symbols		
A	Dispersion constant	J
A_c	Cross-sectional area of cuvette	m^2
h_{fg}	Latent heat of vaporization	J/kg
k_s	Thermal conductivity of quartz	W/m K
k_l	Thermal conductivity of pentane	W/m K
k_{B}	Boltzmann constant	$\mathrm{J/s{\cdot}m^2{\cdot}K^3}$
m	Mass of a single molecule	kg
M	Molar mass	kg/mol
$\dot{m}''$	Interfacial mass flux	$\mathrm{kg/m^2s}$
P	Pressure	Pa
ρ	Density	$\mathrm{kg/m^3}$
p_o	Outside perimeter of cuvette	m
$\bar{R}$	Universal gas constant	J/kg·K
T	Temperature	K
V_l	Molar volume	$\mathrm{m^3/mol}$
l_T	translational length ratio	-
Greek Symbols		
δ	Film thickness	m
ϵ	Emissivity	-
κ	Film curvature	$\mathrm{m^{-1}}$
λ	Wavelength of light	
Π	Disjoining pressure	Pa
σ	Surface tension	N/m
σ_B	Stefan-Boltzmann constant	$\mathrm{W/m^2{\cdot}K^4}$
α_c	Condensation coefficient	-
α_e	Evaporation coefficient	-
β	Ratio of evaporation and condensation coefficients	-
α_{TST}	Average condensation coefficient (Transition State Theory)	-
Subscripts		
i	i^{th} point along the interface	
max	Maximum value	
min	Minimum value	
sat	Saturation	
w	Wall	
∞	Surrounding	
Superscripts		
l	Liquid	
v	Vapor	

1. Introduction

Liquid vapor phase change is widespread in various scientific and industrial applications including space technologies [1–5], atmospheric science [6, 7], biology [8–10] and agriculture [11–14]. Modeling phase change during evaporation/condensation is a complex multiscale problem and kinetic theory is a widely used modeling strategy. Hertz [15] treated the vapor as an ideal gas with molecular velocities described by a Maxwell-Boltzmann distribution and developed an expression for mass flux of vapor molecules passing through an imaginary plane referred to as the Kinetic Theory Plane, KTP:

$$\dot{m}'' = \sqrt{\frac{m}{2\pi k_{\mathrm{B}}}}\left(\frac{P^{v}}{\sqrt{T^{v}}}\right) \tag{1}$$

where $\dot{m}''$ is the mass flux, m is the mass of a single vapor molecule, k_{B} is the Boltzmann constant, T^{v} is the vapor temperature, P^{v} is vapor pressure. It is common to assume a sharp interface separates the liquid and vapor phases and the KTP is "just inside the vapor" [16]. The position of KTP (S_{KTP}) relative to the location of the interface (S) is not universally established [17]. An alternative is a diffuse interface model that locates S and S_{KTP} at either end of the interfacial region where the properties are equal to the bulk phase as shown in Figure 1 [18]. Net phase change is an algebraic sum of simultaneous condensation and evaporation fluxes emanating from the bulk vapor and liquid, respectively. The vapor flux $\dot{m}_{v}''$ is calculated using equation 1 for the vapor temperature T_{i}^{v} at location S_{KTP}. The evaporation flux from the liquid $\dot{m}_{l}''$ is not as straightforward. Many studies approximate this flux by envisioning a hypothetical equilibrium state where the temperature is T_{i}^{l} which is the liquid-side interface temperature at saturation pressure P_{s}. In this hypothetical equilibrium state, the flux from the bulk liquid is by definition equal to the flux from the bulk vapor thereby enabling an approximation of $\dot{m}_{l}''$. This approximation is common to most kinetic theory models and is discussed in detail in prior publications [17, 18]. Evaporation and condensation occur simultaneously and the algebraic difference between the two is the net phase change flux [19–22]. The first term, shown in red, represents evaporation ($\dot{m}_{l}''$) and the second term, shown in blue, represents condensation ($\dot{m}_{v}''$):

$$\dot{m}'' = \sqrt{\frac{m}{2\pi k_{\mathrm{B}}}}\left[\frac{P_{s}(T_{i}^{\,l})}{\sqrt{T_{i}^{\,l}}} - \frac{P_{i}^{v}}{\sqrt{T_{i}^{\,v}}}\right] \tag{2}$$

where P_{i}^{v} is the vapor pressure, and $P_{s}(T_{i}^{\,l})$ is the equilibrium saturation pressure at $T_{i}^{\,l}$. This approach to computing a net evaporation or condensation has two shortcomings. First, reflection of vapor molecules at the interface is neglected. Second, evaporation and condensation fluxes are based on the superposition of two different equilibrium states. The current study revisits these long-standing simplifications and analyzes their impact on heat and mass transfer during phase change.

When a vapor molecule is incident on the liquid-vapor interface, it may interact with the condensed phase in three ways. The molecule may be (1) accommodated into the liquid phase (condensation), (2) reflected back into the

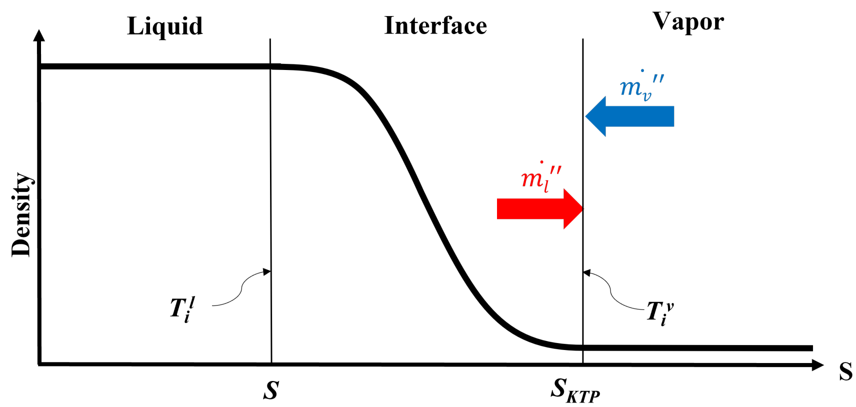

Figure 1: Schematic showing liquid, vapor, and diffuse interface during liquid-vapor phase change. S and S_{KTP} are located in the diffuse region where the local densities change from liquid to vapor. The evaporation ($\dot{m}_l''$) and condensation ($\dot{m}_v''$) fluxes are computed at S_{KTP}

vapor phase, or (3) displace another molecule from the liquid phase. These three scenarios are illustrated in figure 2. Reflection of vapor molecules results in the mass flux at surface S to deviate from equation 2. The discrepancy between the theoretical flux and measured rates of evaporation and condensation led to the introduction of coefficients for evaporation and condensation, α_e and α_c, respectively [23–25]:

$$\dot{m}'' = \sqrt{\frac{m}{2\pi k_{\text{B}}}}\left[\alpha_e \frac{P_s(T_i^{\,l})}{\sqrt{T_i^{\,l}}} - \alpha_c \frac{P_i^v}{\sqrt{T_i^{\,v}}}\right] \tag{3}$$

α_e and α_c have theoretical limits of 0 and 1. A value of 1 denotes total accommodation into the new phase and a value of 0 denotes total reflection.

Schrage [26] modified this kinetic model by considering a drift velocity in the bulk vapor superimposed on the Maxwell-Boltzmann distribution. A drift velocity correction factor, $D(\xi)$, was added to the condensation term:

$$\dot{m}'' = \sqrt{\frac{m}{2\pi k_{\text{B}}}}\left[\alpha_e \frac{P_s(T_i^{\,l})}{\sqrt{T_i^{\,l}}} - D(\xi)\alpha_c \frac{P_i^v}{\sqrt{T_i^{\,v}}}\right] \tag{4}$$

$$D(\xi) = \exp(\xi^2) - \sqrt{\pi}\xi\left[1 + \text{erf}(\xi)\right] \tag{5}$$

where ξ is the ratio of macroscopic drift velocity (w_o) to the most probable velocity of the vapor molecule (v_{mp}). Drift velocity can be expressed as $w_o = \dot{m}''/\rho_v$. For $\xi < 10^{-3}$, equation 4 reduces to the simplified Schrage model:

$$\dot{m}'' = \frac{2}{2-\alpha_c}\sqrt{\frac{m}{2\pi k_{\text{B}}}}\left[\alpha_e \frac{P_s(T_i^{\,l})}{\sqrt{T_i^{\,l}}} - \alpha_c \frac{P_i^v}{\sqrt{T_i^{\,v}}}\right] \tag{6}$$

The Schrage model is applicable to flat liquid-vapor interfaces far from solid substrates. Phase change can be affected by the presence of a solid substrate through mechanical forces arising from disjoining (intermolecular effects)

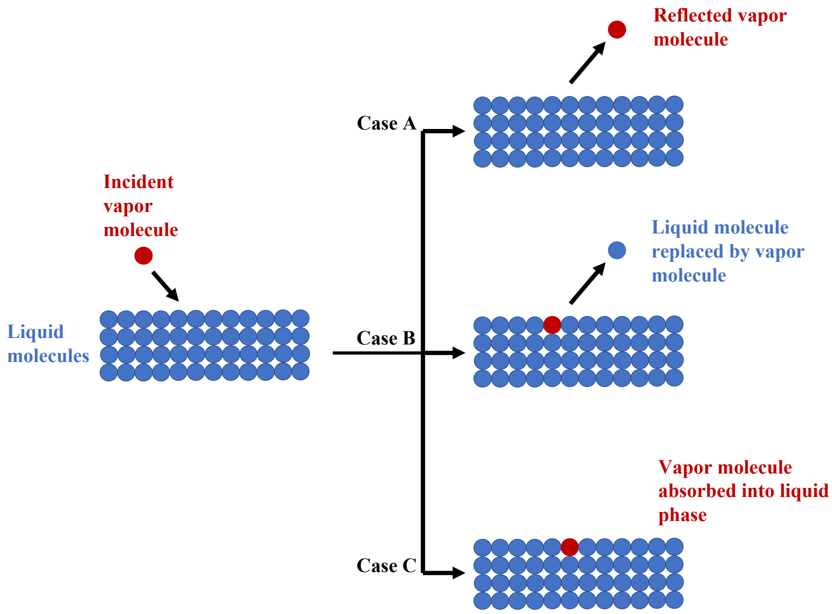

Figure 2: Different ways in which an incident vapor molecule can interact with liquid molecules: (A) Vapor molecule gets reflected off the interface. (B) Vapor molecule displaces a liquid molecule undergoing simultaneous evaporation and condensation, (C) Vapor molecule is absorbed into the liquid phase and undergoes condensation.

and capillary pressure (interfacial curvature) [27]. Wayner [28] incorporated these effects using Clausius-Clapeyron equation and integrating the Gibbs-Duhem equation over small intervals where fugacity change and vapor pressure changes are equal. The work of Wayner [28] has been reformulated by Bellur et al. [18] as:

$$\dot{m}'' = \left(\frac{2\alpha_c}{2-\alpha_c}\right)\frac{P_i^v}{\sqrt{\pi}v_{mp}}\left[\beta W\sqrt{\frac{T_i{}^v}{T_i{}^l}} - 1\right] \tag{7}$$

where, $\beta = \alpha_e/\alpha_c$ and W is a ratio of the pressures, $P_s(T_i^l)/P_i^v$, that incorporates curvature-induced pressure and disjoining pressure.

$$W = \frac{P_s(T_i{}^l)}{P_i^v} = \frac{P_{\text{sat}}^v}{P_i^v} + \frac{\rho_{\text{sat}}^v h_{fg}}{P_i^v}\left(1 - \frac{T_i^v}{T_i^l}\right) + \left(\frac{T_i^v}{T_i^l}\right)\left(\frac{\rho_{\text{sat}}^v}{\rho^l}\right)\left(\frac{\Pi + P_c}{P_i^v}\right) \tag{8}$$

Π is disjoining pressure and P_c is the capillary pressure of the liquid given by the product of surface tension (σ) and curvature (κ). Equation 7 is equivalent to that derived by Wayner [28], but is presented in a form where each term is non-dimensional and α_e and α_c are not assumed to be equal. There are three unknowns in equation 7, the liquid side temperature (T_i^l) and coefficients α_e and α_c. To bring closure, it is commonly assumed that $T_i^l = T_i^v$; that is, the saturation conditions at the liquid interface is the same as the far field vapor equilibrium temperature. The ramifications of this assumption are discussed in Bellur et al. [18] and Chakrabarti et al. [5]. An additional assumption is that $\alpha_e = \alpha_c$. There is no physical evidence to suggest this latter assumption is appropriate [5, 25, 29–33]. These two assumptions leaves α_c as the only unknown variable in the kinetic formulation, which often becomes a tuning parameter used to match the computed rate of phase-change to experimental data. As a result, there are significant discrepancies in reported values of the condensation coefficient, also known as an accommodation coefficient. The reported values of the coefficients for water range from 0.01 to 1 [25, 34–36]. Badam et al. [37] showed that assuming equality of evaporation and condensation coefficients required an order of magnitude adjustment to match experimental and theoretical values. Kryukov and Levashov [38] reinforced this argument by demonstrating that the uncertainty in calculating these coefficient values is significantly greater when the coefficients are assumed to be equal than when they are considered distinct. Montazeri et al. [39] reported a 50% variation between evaporation and condensation coefficients using molecular dynamics simulations of phase change in adsorbed water films on top of nanostructures. Meland et al. [40] also reported inequality of evaporation and condensation coefficients for an LJ-spline fluid near equilibrium. The potential inequality of coefficients is also impacted by parameters on a molecular level such as the structure of the interface [41, 42], polarity of molecules undergoing phase change [34], and presence of contaminants on non-renewing interfaces [20, 33, 43–46]. In summary, forcing $\alpha_c = \alpha_e$ is a convenient simplifying assumption to attain closure of the kinetic model, but is not based on a mechanistic understanding. The present study provides a new methodology to test the equality of the two coefficients using high-quality data from the Constrained Vapor Bubble experiments [47, 48] conducted on the International Space Station.

2. Constrained Vapor Bubble experiments

The Constrained Vapor Bubble (CVB) experiment [2, 47, 49–52] was envisioned as an ideal wickless grooved heat pipe to investigate microscale heat transfer and interfacial phenomena. The setup consisted of a quartz cuvette with an internal dimension of 3 mm x 3 mm. An overview of the experiment setup can be seen in figure 3(a). The cuvette was evacuated and partially filled with n-pentane. The liquid fully wets the interior surface of the cuvette and forms a central bubble. During the experiments, one end of the cuvette was heated while the other was cooled. Liquid evaporated at the heated end into vapor, which was transported through the central bubble to the cooler end where it condensed. The condensed liquid wicked up the corners and was then transported back to the heated end through capillarity. Temperatures along the axis of the cuvette were measured by thermocouples that were embedded in one wall of the cuvette. Two types of imaging data were obtained. The first was a macro view of the cuvette. The second were high magnification (50x) interferograms that were used to determine the curvature of the liquid-vapor interface. The interferograms were 'stitched' together to obtain an end-to-end perspective of the liquid film curvature. The CVB tests were conducted in a microgravity environment on board the International Space Station (ISS) and are described at length in prior publications [2, 47, 49–52]. Temperature, heater power, and imaging data from these experiments are available from the NASA Physical Sciences Informatics (PSI) data base [53].

Of particular interest here is the fact that the CVB is a closed system and the net mass flux across the liquid-vapor surface must be zero at steady state. In other words, whatever amount of liquid evaporated at the heated end must condense at the cold end. This provides a unique closure condition that enables independent calculation of α_e and α_c. The high quality data from the ISS experiments conducted in the absence of gravity provides the perfect sandbox to test the equivalence of α_e and α_c. The following sections describe analysis of the experimental data, multiscale model and the of the heat and mass balances to calculate the coefficients.

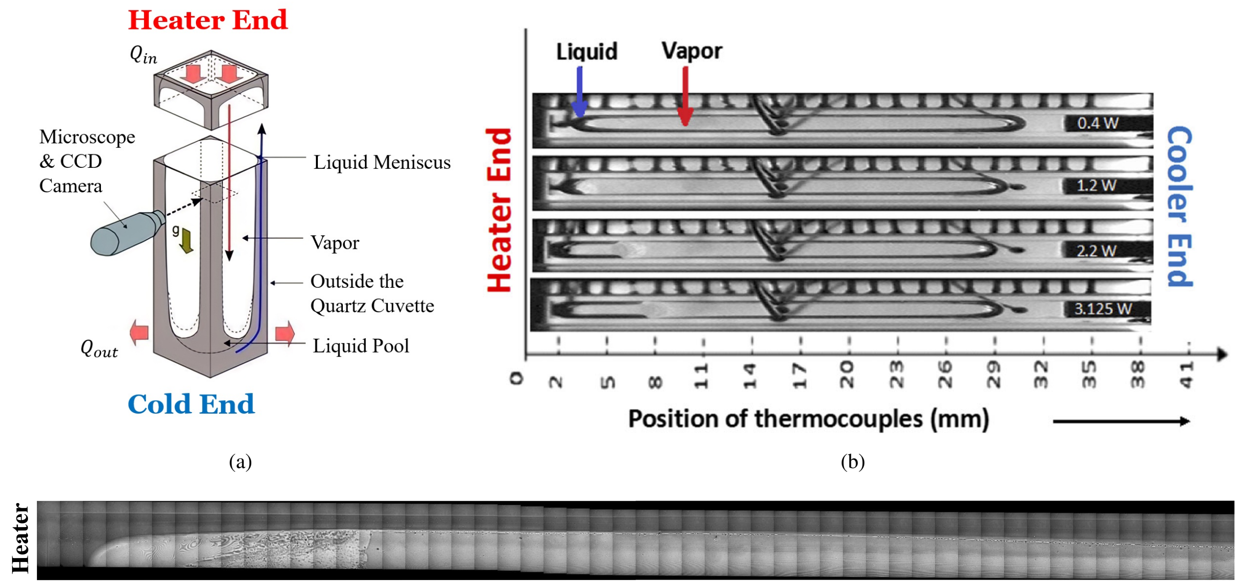

(a) (b)

(c)

Figure 3: (a) Schematic of the CVB experimental setup. (b) Sample low magnification(10X) images showing steady, equilibrium bubble shapes for different heater inputs. (c) High magnification (50X) “stitched” images that are used the present study for reconstruction of the bubble as explained in section 3.1. Images were obtained from the NASA PSI database [53].

3. Image Analysis and Liquid Surface Reconstruction

Monochromatic light (λ = 546 nm) is incident on the closed cuvette during the CVB experiment which is partly reflected at both solid-liquid and liquid-vapor interfaces. A phase shift is created between the two reflecting light rays leading to interference. A fringe pattern with constructive and destructive interference is produced for a curved surface, where the film thickness is gradually changing (figure 4). These fringe patterns are observed in the 50x images (figure 3(c)). A 3-dimensional geometry of the liquid domain is reconstructed using a custom image processing routine where the pixel intensities along a line scan (blue arrow in figures 4, 5) in the fringe pattern images are converted to a film thickness profile. The authors have discussed the specifics of the image processing in a previous publication [5]. The film thickness profiles are obtained for the entire surface of the bubble when there is no input (0 W) from the heater end. The current study is limited to the shape obtained from the 0W setting due to a lack of high-resolution data for cases with higher heat settings. The final outcome of this step is a computational liquid-solid domain representing 1/8th of the CVB cross-section symmetric about 3 axes as shown in figure 4. The next step involves the implementation of appropriate thermal boundary conditions to calculate the two coefficients.

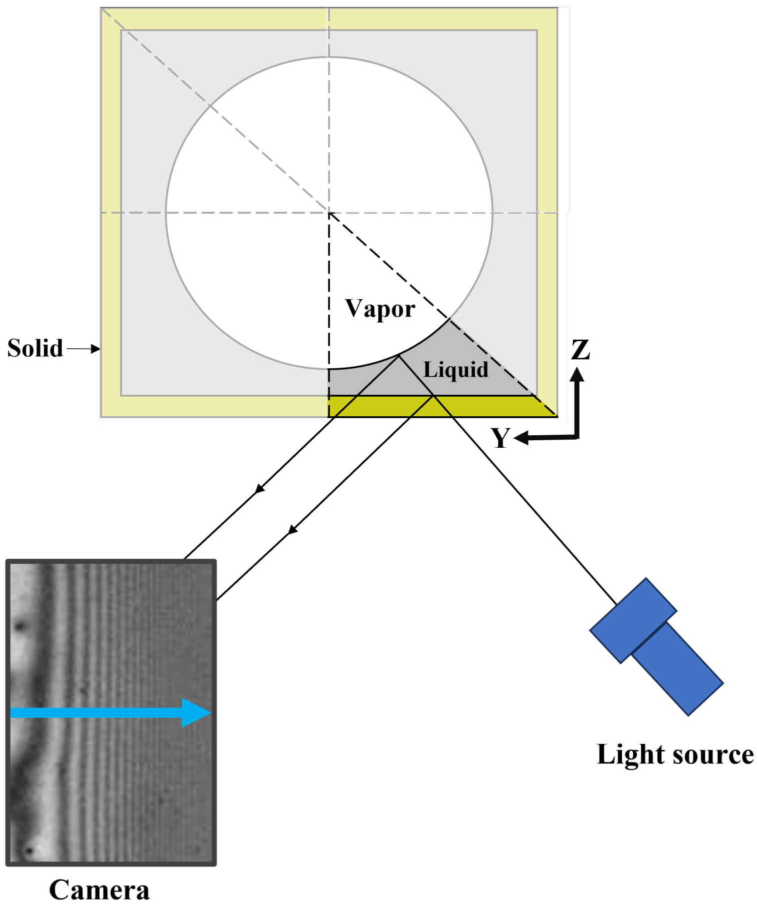

Figure 4: The diagram above is a schematic description of the reflection of a monochromatic light ray from an incident source at the solid-liquid and liquid-vapor interfaces of the 2D cross section of CVB experimental setup. Interaction of the two reflected waves for incident rays at different points along the curved liquid-vapor interface of the bubble forms interference patterns captured by the camera in the experimental setup

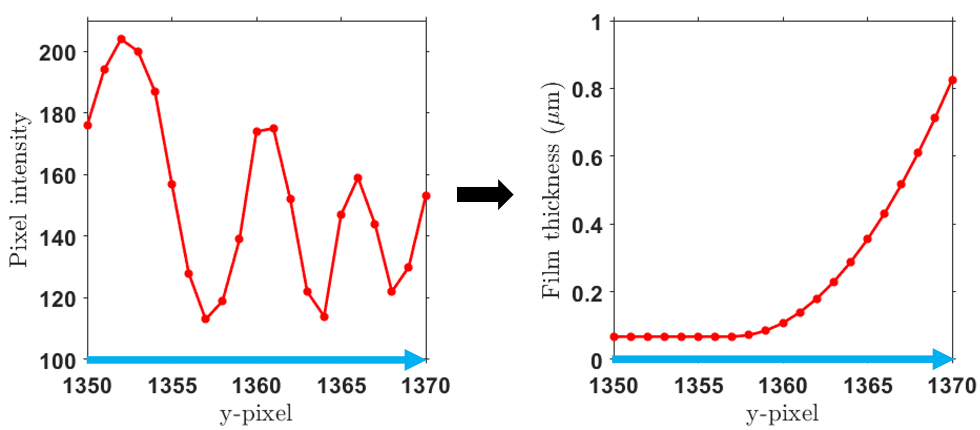

Figure 5: Line scans in the positive y direction (blue arrow in Figure 4), provides a 2D pixel intensity plot along the same direction. The pixel intensity is converted to a film thickness plot along the y-direction using the methodology established in [5].

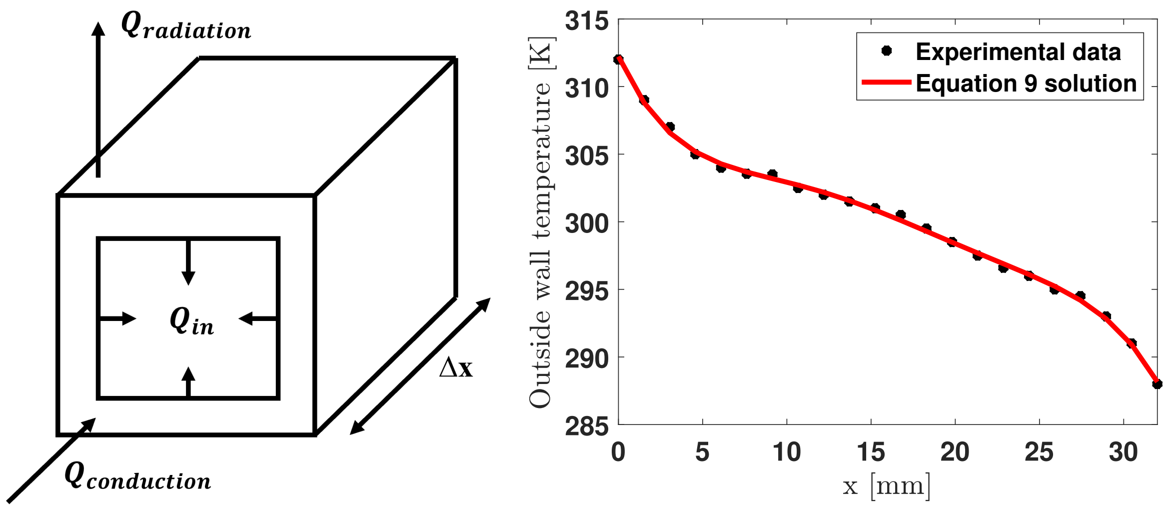

(a) (b)

Figure 6: (a) Sectional schematic of heat balance along the wall where for every unit length Δx heat conducted axially ($Q_{conduction}$) balanced by heat loss due to radiation ($Q_{radiation}$) and heat lost into the fluid (Q_{in}). (b) Experimental temperature measurements at the outside wall are used to obtain optimized emissivity and surrounding temperature values. Equation 9 is solved and compared to the experimental data. The emissivity and surrounding temperatures are then used as boundary condition parameters in the computational analysis.

4. Thermal boundary conditions in the CVB

4.1. Outer wall boundary conditions from evacuated "dry" tests

During the CVB experiments a fully evacuated cuvette was heated in order to determine the outer wall heat transfer to the ISS environment. In the absence of natural convection in microgravity, the dominant mechanism is radiation [47, 54]. Heat conducted axially was balanced by radiative heat transfer to the environment and heat transferred into the fluid (when present) as shown in figure 6(a). The resultant heat balance is given by:

$$\underbrace{-k_s A_c \frac{d^2T(x)}{dx^2}}_{\text{conduction}} = \underbrace{\sigma_B \epsilon p_o (T(x)^4 - T_\infty^4)}_{\text{radiation}} + Q_{\text{in}} \tag{9}$$

Here, Q_{in} is the heat input to the liquid. For an evacuated cell, Q_{in} is assumed to be negligible. Emissivity ϵ and the ambient temperature T_∞ were determined by fitting equation 9 to the experimentally recorded temperatures as shown in figure 6(b). A 4th order Runga-Kutta method (ODE45 in Matlab™) was used to solve equation 9 subject to an experimentally known heater setting and cooler side temperature. The radiation view factor was taken to be unity. The resulting values for ϵ and T_∞ were found to be 0.773 and 293 K, respectively. This correlates well with the average ambient temperature on board the ISS during the CVB testing; also reported to be 293 K [54].

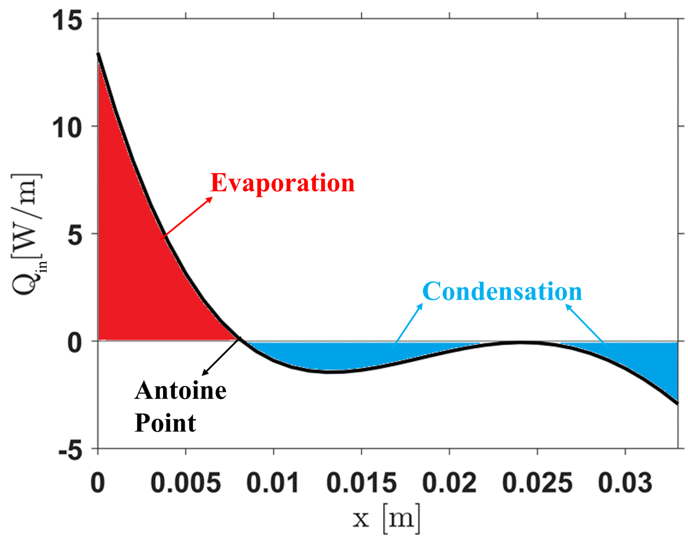

Figure 7: The profile of heat flow rate per unit length (Q_{in}) along the outer wall with Q^{+}_{in} represented by the red shaded area representing evaporation. The plot obtained is for a heater setting of 0.2W. Q_{in} becomes zero at the Antoine point.

4.2. *Inner wall conditions from "wet" tests*

Using the values for ϵ and T_∞ determined in section 4.1, the discrete (i.e., local) heat transferred into the fluid (Q_{in}) during the pentane-filled cuvette test was computed. Figure 7 illustrates $Q_{in}(x)$ for the 30 mm long cuvette at 0.2 W heater power as computed from equation 9. The net heat transfer to the fluid is zero when operating at steady state conditions. However, this is split into two separate integrals that are equal and opposite: heat addition (evaporation) and heat rejection (condensation). By considering just the positive values of $Q_{in}(x)$, the net heat addition to the cuvette (Q^{+}_{in}) is calculated. This is effectively just the area of the red colored evaporation section in figure 7. This particular feature is critical to obtaining a non-zero integral value to calculate α_c as discussed in section 5.

$$Q^{+}_{in} = \int Q_{in}(x) \cdot dx \tag{10}$$

5. Multiscale Model

The liquid film thickness in the curved interfacial domain reconstructed in Section 3 has length scales ranging from millimeters to nanometers. For computational efficiency, the domain is divided into macroscale and microscale submodels. The heat and mass transfer calculations are performed separately for the submodels and are coupled together using the methodology explained in the upcoming subsections.

5.1. Macroscale submodel

The liquid-solid domain, reconstructed and comprising of 5.7 million mesh cells, is implemented in Ansys Fluent. In figure 8, the liquid domain is depicted in gray, while the solid wall is represented in yellow, with the hot and cold end apex tips at x = 5 mm and 29.7 mm respectively. Assuming laminar flow within the liquid, a no-slip boundary condition is applied to the entire inner solid wall. Experimentally known heater setting of 0.2 W used as the thermal boundary condition at the hot end. The cold end is maintained at a constant temperature of 288 K, consistent with the experimental setup with an anticipated error of less than 0.5 K [3]. Symmetry boundary conditions are employed as appropriate. A radiative heat flux boundary condition is implemented at the outer wall, utilizing ϵ and T_∞ derived from the dry heat balance (section 4). Thermophysical properties for pentane are obtained from the NIST website [55], while the density and thermal conductivity of quartz are set at 2719 kg/m^3 and 1.4 W/mK respectively. Considering a steady-state near-equilibrium bubble, constant vapor properties are assumed and only the liquid domain is modeled. To model phase change at the curved interface, a single-cell thick layer of mesh cells in the liquid domain, adjacent to the interfacial surface is marked and designated as the "active region". User Defined Functions (UDFs) are utilized within this region to calculate local mass flux based on a phase change model for curved liquid-vapor interfaces (equation 7) with locally queried liquid properties and constant vapor properties. Latent heat flux is then determined by multiplying the mass flux with the enthalpy of evaporation of pentane. These computed fluxes act as volumetric source or sink terms in the active region to account for evaporation and condensation. Equation 7 needs an input for α_e and α_c. So, as a starting point, the value of α_c is initially set to be equal to α_e with a value of 0.5, making $\beta = 1$. The temperature and pressure for vapor are determined using a similar methodology to that of Chatterjee et al. [47]. Wall temperature is extracted at the x-location where the Q_{in} crosses zero; i.e. the Antoine point. The temperature at this point is considered to be the vapor temperature. The vapor pressure at the Antoine point is:

$$\log_{10}(P_i^v) = C_1 + \frac{C_2}{T_i^v + C_3} \tag{11}$$

C_1, C_2 and C_3 are constants equal to 7.00877, 1134.15 and 238.678 respectively for pentane [47]. Surface tension is modeled as a linear function of liquid temperature at the interface (T_i^l),

$$\sigma = \sigma_0 + \gamma\left(T_i^l - T_0\right) \tag{12}$$

where σ_0 is 0.0476 N/m at $T_0 = 300\,\text{K}$ and $\gamma = -10^{-4}$ N/m-K [55].

The macroscale domain is truncated at a liquid film thickness of 10 μm resulting in a cutoff plane (figure 8). Initially, a zero heat and mass flux boundary condition is applied at the cut-off plane. Steady-state mass, momentum, and energy equations are solved using the SIMPLEC pressure-velocity coupling in Ansys Fluent. The temperatures

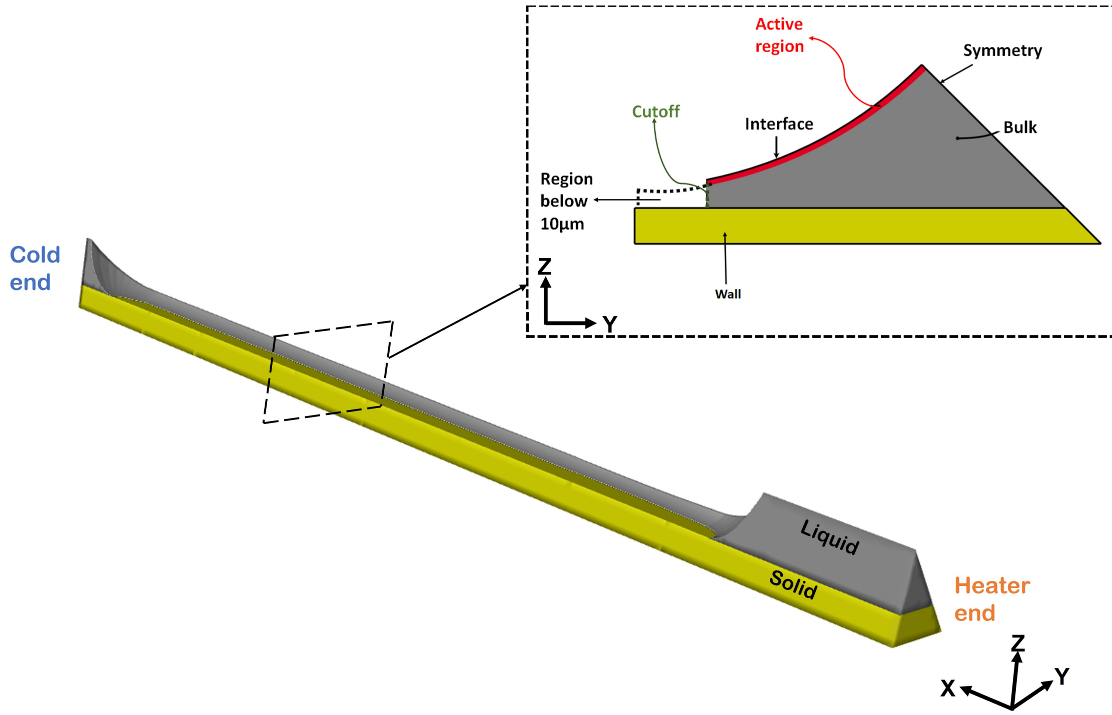

Figure 8: The reconstructed 1/8th section of the CVB experiment showing the liquid pentane and quartz solid with the location of the heater and the constant cold temperature [5]

extracted from the inner wall are used to determine heat and mass flux contributions from the cut-off thin film below 10 μm, as detailed in the following section.

5.2. Microscale submodel

A microscale thin film submodel is used to solve for net mass and heat transfer in the truncated region and is coupled with the macroscale submodel. The thin film submodel is centered around a heat balance, wherein the conduction heat flux from the solid wall is equal to the phase change heat flux. The temperature gradient through the film (z-direction) is significantly larger than that in the x and y directions due to orders of magnitude difference in length scales. Hence, a 1D heat transfer approximation is applied in the microscale thin film [5]:

$$h_{\mathrm{fg}}\dot{m}'' = -\frac{k_l}{\delta}\left(T_w - T_i^l\right) \tag{13}$$

Equation 13 is a balance of latent heat flux at the curved interface and 1D conduction through the pentane liquid using Fourier's law. Employing the film thickness (δ) obtained from image processing for the profile below the 10 μm cutoff and results from the macroscale submodel, a new local interfacial mass flux ($\dot{m}''$) and T_i^l and is calculated at each point on the microscale thin film. The process starts at the cutoff and proceeds in a direction of reducing film thickness. The interfacial temperature at the cutoff (T_i^l) and the wall temperature profile (T_w) is readily available

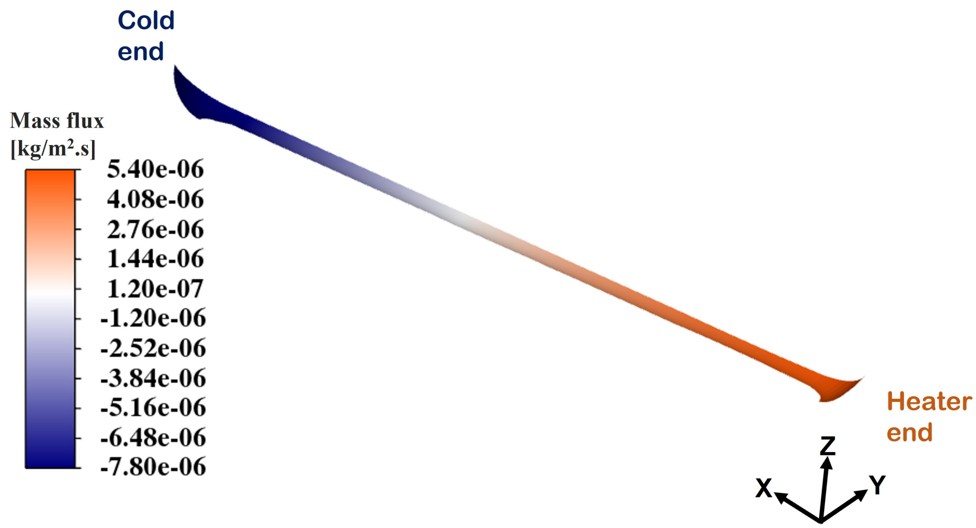

Figure 9: Mass flux profile of the interfacial region of the CVB domain obtained by coupling the thin film model with the macroscale model.

from the macroscale submodel. This is used to calculate a new value of T_i^l and $\dot{m}''$ at an adjacent y location based on equation 13. This process is repeated until the symmetry plane (y = 0 mm) is reached or the $\dot{m}''$ becomes negligible. This process is repeated for multiple axial locations along the CVB. The mass flux profiles in the microscale regions (<10 μm) are then extracted and integrated over the corresponding film length to obtain the mass and heat flow rate per unit length along the axis. This can now be fed back into the macroscale submodel as a mass flow boundary condition, effectively relaxing the previously made no-mass flux at the cutoff assumption and establishing a robust 2-way coupling between the submodels.

The macroscale and microscale submodels are solved iteratively to resolve interfacial mass fluxes in the entire multiscale domain. The solution begins in the macroscale submodel assuming no evaporation contribution from the thin film. The interface temperature at the cutoff and inner solid wall temperatures from the macroscale submodel are then used as inputs in the microscale model. The heat and mass flux contribution from the microscale model is fed back into the macroscale model in successive iterations. The coupled multiscale model is iteratively solved until the change in inner wall temperature (T_w) is less than 0.1 % between consecutive iterations. Coupling the thin film submodel with the macroscale submodel yields a continuous, smooth mass flux distribution along the entire surface (figure 9). This coupled approach eliminates the need for guessed or arbitrary matching conditions, relying solely on experimental inputs. Additional detail on this modeling strategy can be found in the authors' prior publication [5]. The interfacial temperatures (T_i^l), mass fluxes and other geometric properties obtained from the multiscale model are used as inputs to mass and energy conservation equations to determine the values of condensation (α_c) and evaporation coefficients (α_e) using mass and energy conservation constraints as described in the next section.

6. Determining α_c and β

From the multiscale model results, the values of temperatures, pressures, film thickness, and curvature are first queried at all the data points along the interface. Using these parameters, the mass flux m'' is determined along the interface using equation 7. Since the CVB experimental setup is a closed system, the net mass flux across the interface is zero. This provides the first constraint for calculation of the coefficients:

$$\dot{m} = \int_s \left[\frac{2\alpha_c}{2-\alpha_c} \frac{P_i^v}{\pi v_{mp}} \left[\beta W \sqrt{\frac{T_i^v}{T_i^l}} - 1 \right] \right] dA = 0 \tag{14}$$

α_c and $\sqrt{\frac{m}{2\pi k_B}}$ are uniform on the entire surface and equation 14 reduces to:

$$\int_s \left[\beta W \sqrt{\frac{T_i^v}{T_i^l}} - 1 \right] dA = 0 \tag{15}$$

β obtained from equation 15 is a single value that applies to the entire interfacial domain. α_c is obtained from an evaporation-only energy balance. The net heat added into the CVB domain obtained from equation 10 (Q_{in}^+) must equal the net mass flux integrated over just the positive values of $\dot{m}''$ multiplied by the local latent heat of evaporation (h_{fg}) as shown in equation 16:

$$Q_{\text{in}}^+ = \int h_{fg} \dot{m}'' dA \tag{16}$$

Using the value of β from the first constraint (equation 15) for mass flux in equation 16, the second constraint is derived to compute a constant α_c for the entire interfacial domain:

$$Q_{\text{in}}^+ = h_{fg} \frac{2\alpha_c}{2-\alpha_c} \sqrt{\frac{m}{2\pi k_B}} \int \left[\beta W \sqrt{\frac{T_i^v}{T_i^l}} - 1 \right] dA \tag{17}$$

The algorithm to iteratively compute α_c and β is shown in figure 10. The process is starts with initial guessed values. The multiscale model is used to obtain local thermophysical properties and a map of mass flux along the entire domain. The values of α_c and β are computed from equations 15 and 17. The calculated set of α_c and β values are fed back into the multiscale model and iterated till the change in both α_c and β are less than 0.001 %. The results obtained from this iterative scheme, choice of initial guesses and the sensitivity of the value of β are discussed in the proceeding section.

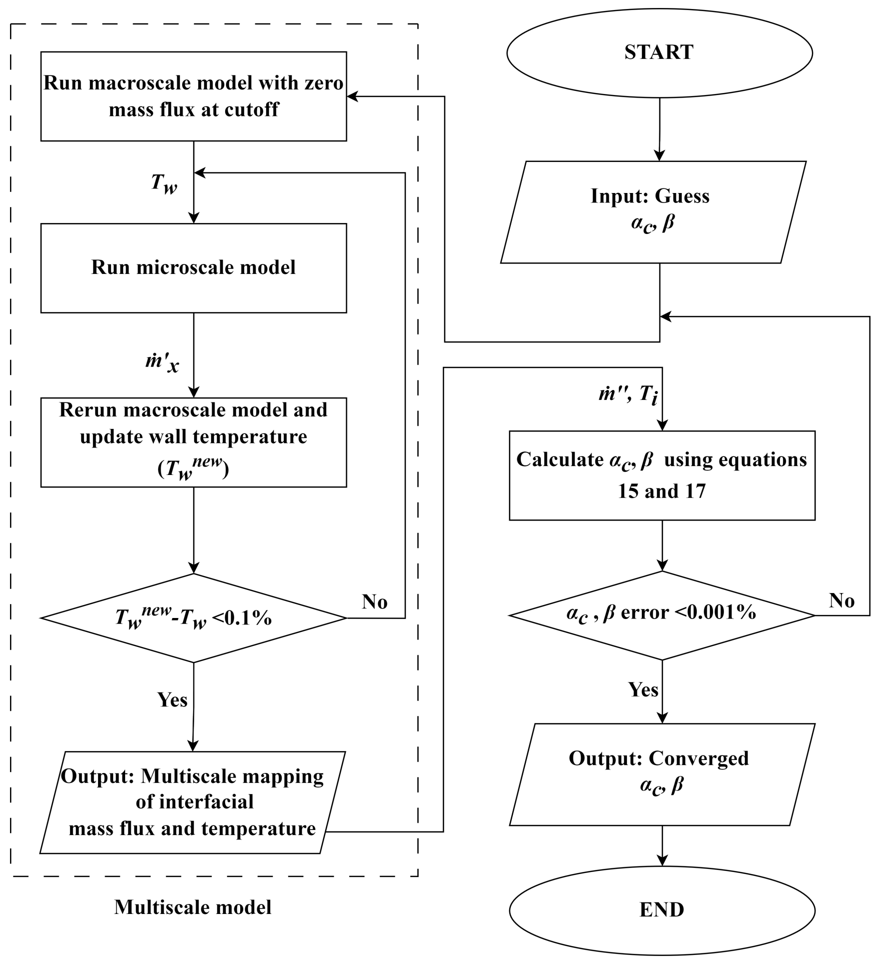

Figure 10: Flow chart explaining entire methodology used for obtaining α_c and β

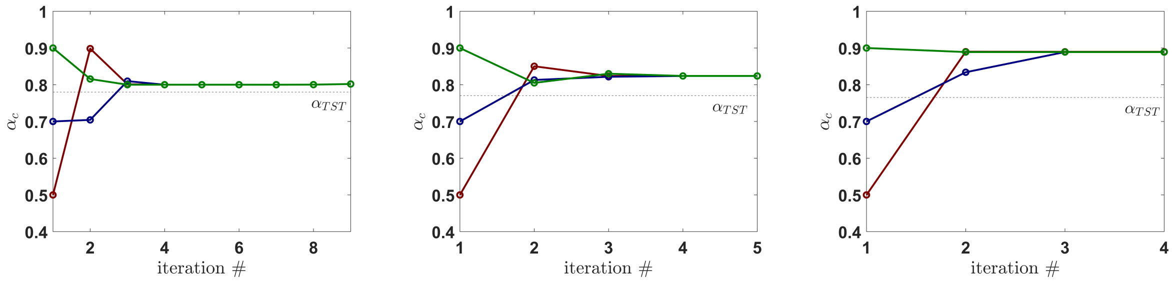

(a) 0.2 W (b) 0.4 W (c) 0.6 W

Figure 11: The computed values of α_c values in each iteration as explained in section 2.6 are plotted against the iterative loop number. α_c convergence for different initial guess at (a) 0.2 W, (b) 0.4 W and (c) 0.6 W heater setting are shown above.The red, blue, and green connectors are not interpolants. They are used to explain the propagation of the solution over different iterations. A horizontal line is drawn to represent expected α_{TST} obtained from transition state theory(TST). Although the obtained α_c and α_{TST} are within 2% for the 0.2 W heater setting. the difference between the converged α_c and α_{TST} is seen to increase with heater settings of 0.4 W and 0.6 W.

7. Results and discussion

7.1. Converged coefficient values

Based on the methodology described in the previous section, the results for converged values of α_c and β are calculated to be 0.801±0.031 and 0.996±0.001 respectively for the 30 mm cuvette set to 0.2 W . The uncertainty in these values are due to both experimental inputs and numerical modeling. The uncertainty in thermocouple measurement was reported during the CVB experiments to be ±0.5 K along with a thermocouple location uncertainty of ±0.1 mm. The propogated error in T_i^l while using the multiscale model is 0.53 K . The propagated error as a result of all the sources mentioned above results in an uncertainty of around 0.1% in β and 3.9% in reported values of α_c. The iterative scheme is stable and reproducible. The values of α and β calculated are independent of the initial guess. Figure 11(a) shows that the same converged values are obtained even when a wide range of the initial guess for α_c are used at different heater settings.

For validation, the calculated condensation coefficient α_c is compared with that obtained by Nagayama and Tsuruta [56] (α_{TST}) using transition state theory (equation 18). To the best of the author's knowledge, this is the current state-of-the-art formulation for calculating the coefficients and agrees well with several other studies [18]. α_{TST} was estimated using the saturation properties of liquid and gaseous pentane using temperatures from the Antoine point as explained in section 5.1.

$$\alpha_{\text{TST}} = (1 - l_T)\exp\left(\frac{-1}{2l_T - 1}\right) \tag{18}$$

where the translational length ratio $(l_T) = \sqrt[3]{\rho^v_{\text{sat}}/\rho^l_{\text{sat}}}$. This results in $\alpha_{\text{TST}} = 0.782$, which matches the model converged α_c within < 2% at the 0.2 W heater setting. Hence, a new methodology is established for the calculation of evaporation and condensation coefficients independently using mass and energy conservation. The variation between the two coefficients is less than 0.4 %. Although the two calculated coefficients are very close to being equal to each other, the implication of assuming their equality is still not clear. In the next section, the significance of forced equality is explored.

7.2. Convergence by forcing coefficients to be equal

To explore the implications of forced equality, α_e and α_c are calculated using the same iterative method described above (figure 10) with the exception that β is arbitrarily fixed to be a constant value. This would require the calculation of α_c using equation 17 and multiplying α_c with the fixed β value to obtain α_e. The calculated α_c and α_e are plotted against fixed values of β (figure 12). It is observed that α_e and α_c reduce by about 60 % when β is changed from the actual converged value from the previous section (0.996) to the commonly assumed value of unity. While it is certainly enticing to assume $\beta \approx 1$, it must be done so with caution because α_c is extremely sensitive to β. Figure 12 suggests that a variation of almost an order of magnitude in α_c is possible for $< 1\%$ variation in β. This finding explains one of the many reasons for the wide range in reported values of α_c that have spanned many orders of magnitude [25].

To further assess the impact of assuming equality in coefficients, the coupled multiscale model is run using $\beta =$ 1 and it was found that the mass flux values obtained at individual points along the interface vary by about 1.5 %. However, when the local interfacial mass flux is integrated over the interfacial area and multiplied by the latent heat of evaporation to obtain the net evaporative heat flow rate ($\dot{Q}^{+}_{in}$), an underestimation of 12% in the evaporative heat flow rate is observed for cases when β is increased from 0.996 to 1. Hence, assuming equal evaporation and condensation coefficients (as done by many researchers) can induce significant inaccuracies in estimating phase change heat transfer over large liquid-vapor interfacial areas like those in space mission fuel tanks, nuclear power plants, large water bodies etc. This finding adds to the rising concerns regarding the assumption of equal coefficients as discussed in Section 1.

The results for the calculation of coefficients discussed until now are obtained for an equilibrium domain shape of the bubble at 0 W heater setting with boundary conditions at 0.2 W heater setting. The effects of increasing the heater settings for the setup on the calculation of coefficients are explored in the next section.

7.3. Results for higher heater settings

The iterative method described in figure 10 is repeated for a heater settings of 0.4 W and 0.6 W. The calculation procedure described in sections 4-6 are repeated with updated vapor pressure, temperatures along with σ, ϵ and Q_{in} obtained from the dry and wet heat balance for the new heater setting. For 0.4 W, α_c and β equal to 0.824 and 0.996 respectively, are obtained (figure 11(b)). For 0.6 W, α_c and β are calculated to be 0.887 and 0.994 respectively (figure 11(c)). Interestingly, these values deviate from α_{TST} as the heater setting is increased. The deviation between calculated α_c and α_{TST} increases from about 2 % for 0.2 W setting to 6.9 % for the 0.4 W setting and 15 % for the 0.6 W setting.

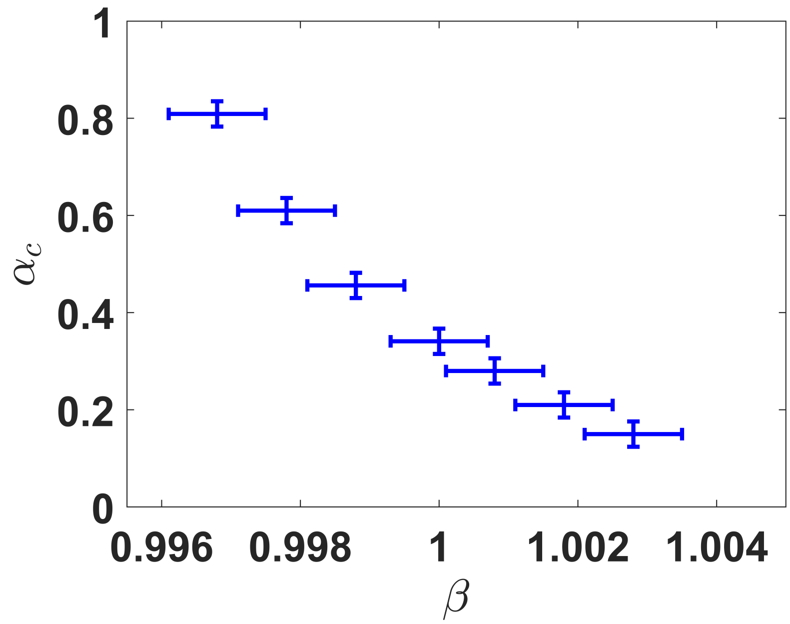

Figure 12: Obtained α_c and α_e values by fixing β as constant. The trend shows that assuming equal α_e and α_c (β = 1)changes the obtained α_c and α_e by about 60% when compared to the coefficients calculated from the iterative scheme mentioned in section 4.1. All values are plotted with error bars estimated in section 4.1

The systemic deviation can be attributed to uncertainties in the interface shape. Absence of high resolution image data and spontaneous oscillations in the liquid film make it difficult to reconstruct interface shapes at higher heater settings. For all cases a 0 W shape is used as standard for the multiscale model and only the boundary conditions relevant to higher heater settings are changed. However, as the heat transferred to the bubble increases, the vapor pressure of the bubble would increase causing it to expand. To account for this increase without actually reconstructing the bubble shape, an area increment factor is introduced to the elemental areas during integral calculations in equation 15 and 17. This area increment can be qualitatively estimated using CVB experimental data. The expansion of the bubble in the y direction is estimated by the change in distance (yellow arrows in figure 13) between the region where the thin film begins(fringe patterns begin to form) and the inner wall. The axial distance is estimated by examining the change in distance between the apex point of the bubble and the inner wall on the heater side (blue arrows in figure 13). An area increase of 6.8 % and 17.1 % is estimated between the 0 W & 0.4 W shapes and 0 W & 0.6 W shapes respectively. Since this area increase was not inherently captured in the multiscale model, the elemental areas are incremented during the numerical integration process when evaluating equations 15 and 17. New values of the coefficients are again calculated with the incremented elemental areas. It is observed that new calculated values of condensation coefficient (α_c^{new}) reduce for both 0.4 and 0.6W cases when the elemental areas are increased. The new values of the calculated condensation coefficient (α_c^{new}) are now closer to that from transition state theory (α_{TST}) upon taking the bubble's area expansion into account at higher heater settings (Table 1). The area increase estimation however becomes difficult

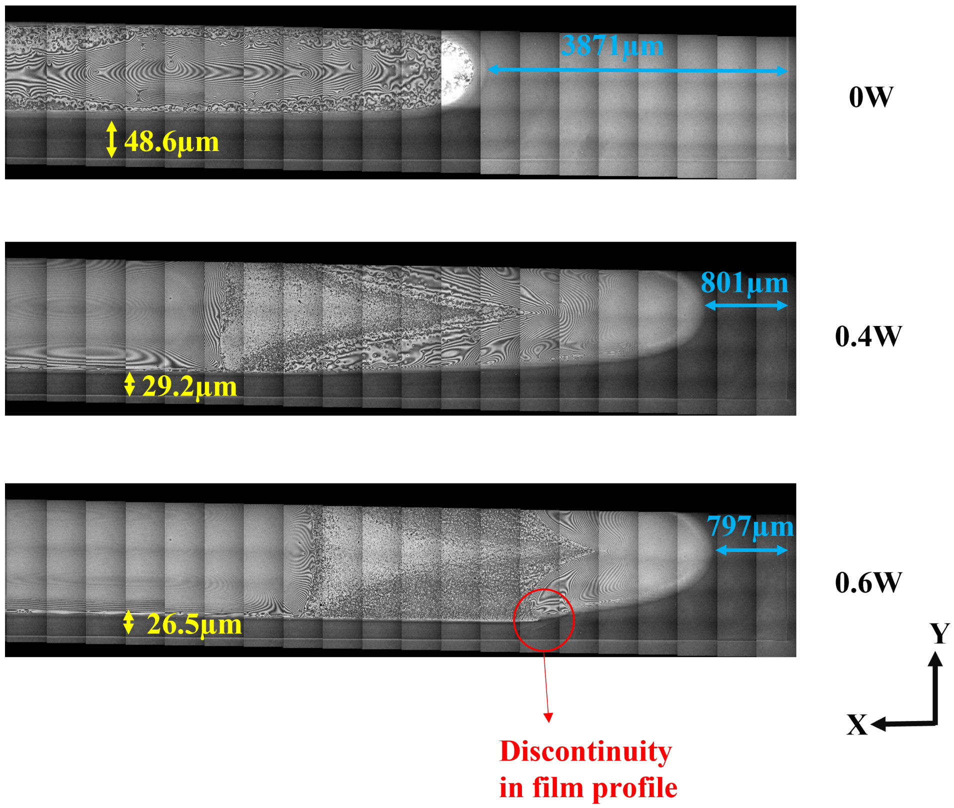

Figure 13: Expansion of the bubble at higher heater settings along the axial(blue) and transverse (yellow) direction. The expansion data is usable until 0.4W. However, at 0.6 W setting, a discontinuity is observed near the heater making it difficult to estimate the expansion.

Table 1: For heater settings of 0.4 and 0.6W, α_c values calculated without adding the area increment (ΔA) are seen to deviate significantly from the expected α_{TST} values. Upon adding ΔA to the area integrals in equation 15,17, this overestimate is reduced and new α_c^{new} is calculated which matched well with α_{TST}

Heater (W)	α_c	α_{TST}	ΔA (%)	α_c^{new}
0.4	0.824	0.770	6.8	0.812
0.6	0.888	0.765	17.1	0.722

at heater settings beyond 0.6 W. This is because of discontinuities observed in the bubble shape (figure 13). This is likely due to instabilities arising from dominant Marangoni forces near the thin film as explained in many prior studies [5, 57]. Higher spatiotemporal mapping of the liquid-vapor interfacial area in future experiments could potentially improve the results described here.

8. Conclusion

Kinetic theory based models for liquid-vapor phase change are popular in literature but contain several longstanding assumptions that have not been well characterized. At the core of all kinetic models is a superposition of two independent pseudo-equilibrium states. This results in two separate terms for condensation and evaporation; each with its own independent coefficient. The net phase change is then simply the algebraic sum of the condensation and evaporation terms. Since the two coefficients are generally unknown, a commonly made assumption is that the evaporation coefficient (α_e) is equal to the condensation coefficient (α_e). To the best of the authors knowledge, there is no physical reasoning for this assumption other than mathematical simplification and closure of equations. This work explores this seemingly ubiquitous simplifying assumption and explores its applicability using the Constrained Vapor Bubble (CVB) experiments conducted on the International Space Station (ISS). The CVB experiment is a closed cuvette that is partially filled with pentane; heated and cooled at opposite ends to form a central bubble. Although it was originally designed for a different purpose, the CVB setup is uniquely suited for testing this fundamental assumption because it is a closed system at steady state where conservation laws dictate that: (1) net mass flux must equal zero and (2) the net heat added to the fluid must equal the total latent heat. This provides the much needed closure conditions to compute both coefficients independently and test the applicability of the simplifying assumption. The study reveals that the two coefficients are close to each other but they are not strictly equal. For the 0.2 W case, $\beta = \alpha_e/\alpha_e = 0.996 \pm 0.001$ and $\alpha_c = 0.801 \pm 0.031$. The value of α_c agrees well with the predicted transition state theory value, α_{TST} [56]. Since $\beta \approx 1$, it may be tempting to force equality by setting $\beta = 1$. This artificially boosts evaporation and this must be compensated by a reduction in α_c. If one does not care about the true value of α_c and merely wishes to use it as a fitting coefficient or as in input in modeling this may not matter. However, the sensitivity between β and α_c is quite dramatic. The value of α_c reduces by almost 50% when β is artificially increased by <0.1%. This reduction in α_c is also accompanied by a similar reduction in α_e and conservation laws are still applicable. More importantly, this reduction in the coefficient reduces the overall latent heat rate considerably. This has the potential to artificially reduce the model predicted throughput of heat transfer devices that rely on phase change such as heat pipes, evaporators, etc.

In conclusion, assuming $\alpha_e = \alpha_e$ reduces the formulation to a single coefficient, called the “accommodation” coefficient. This simplification of the physics has led researchers to reduce the coefficient to a tuning parameter in modeling or empirical fit to experimental data. Assuming $\alpha_e = \alpha_e$ forces an artificially lower value of α_c which in a modeling paradigm limits heat transfer performance of latent heat based devices. This forcing equality in the coefficients is not always applicable. This assumption has the potential to under predict latent heat transfer and artificially limit device performance. This assumption could also be a reason for the discrepancy in prior reported values.

Acknowledgement

The authors would like to thank Ayaaz Yasin for assistance with the computational analysis. This work was supported by a NASA Physical Sciences Informatics Grant (#80NSSC19K0160) and the NSF CAREER award (#CBET-2339757). The authors acknowledge support from the University of Cincinnati through a Graduate Incentive Award for Unmeelan Chakrabarti.

Data Availability

The data that support the findings of this study are available from the corresponding author upon reasonable request.

References

[1] S. Alberts, P. Srikanth, S. H. Collicott, and S. Heister, Numerical approach to measure accommodation coefficients for long-duration spaceflight cryogenic propellants, in: 52nd AIAA/SAE/ASEE Joint Propulsion Conference, 2016, p. 4675. doi:10.2514/6.2016-4675.

[2] A. Chatterjee, J. L. Plawsky, P. C. Wayner, D. F. Chao, R. J. Sicker, T. Lorik, L. Chestney, J. Eustace, J. Zoldak, Constrained Vapor Bubble Experiment for International Space Station: Earth's Gravity Results, Journal of Thermophysics and Heat Transfer 24 (2010) 400–410. doi:10.2514/1.47522.

[3] A. Chatterjee, J. Plawsky, P. Wayner, D. Chao, R. Sicker, T. Lorik, L. Chestney, J. Eustace, J. Zoldak, The Constrained Vapor Bubble (CVB) Experiment in the Microgravity Environment of the International Space Station, in: 49th AIAA Aerospace Sciences Meeting Including the New Horizons Forum and Aerospace Exposition, American Institute of Aeronautics and Astronautics, Orlando, Florida, 2011. doi:10.2514/6.2011-1197.

[4] K. Bellur, E. Médici, M. Kulshreshtha, V. Konduru, D. Tyrewala, A. Tamilarasan, J. McQuillen, J. Leão, D. Hussey, D. Jacobson, J. Scherschligt, J. Hermanson, C. Choi, J. Allen, A new experiment for investigating evaporation and condensation of cryogenic propellants, Cryogenics 74 (2016) 131–137. doi:10.1016/j.cryogenics.2015.10.016.

[5] U. Chakrabarti, A. Yasin, K. Bellur, J. S. Allen, An investigation of phase change induced Marangoni-dominated flow patterns using the Constrained Vapor Bubble data from ISS experiments, Frontiers in Space Technologies 4 (2023) 1263496. doi:10.3389/frspt.2023.1263496.

[6] C. E. Kolb, R. A. Cox, J. P. D. Abbatt, M. Ammann, E. J. Davis, D. J. Donaldson, B. C. Garrett,, C. George, P. T. Griffiths, D. R. Hanson, M. Kulmala, G. McFiggans, U. Pöschl, I. Riipinen, M. J., Rossi, Y. Rudich, P. E. Wagner, P. M. Winkler, D. R. Worsnop, C. D. O' Dowd, An overview of current issues in the uptake of atmospheric trace gases by aerosols and clouds, Atmospheric Chemistry and Physics (2010) 10561–10605.

[7] H. R. Pruppacher, J. D. Klett, P. K. Wang, Microphysics of Clouds and Precipitation, 1998.

[8] M. Fu, T. Yu, H. Zhang, E. Arens, W. Weng, H. Yuan, A model of heat and moisture transfer through clothing integrated with the UC Berkeley comfort model, Building and Environment 80 (2014) 96–104. doi:10.1016/j.buildenv.2014.05.028.

[9] A. Pérez-González, A. Urtiaga, R. Ibáñez, I. Ortiz, State of the art and review on the treatment technologies of water reverse osmosis concentrates, Water Research 46 (2012) 267–283. doi:10.1016/j.watres.2011.10.046.

[10] K. Sefiane, M. E. Shanahan, M. Antoni, Wetting and phase change: Opportunities and challenges, Current Opinion in Colloid & Interface Science 16 (2011) 317–325. doi:10.1016/j.cocis.2011.03.003.

[11] J. D. Valiantzas, Simplified versions for the Penman evaporation equation using routine weather data, Journal of Hydrology 331 (2006) 690–702. doi:10.1016/j.jhydrol.2006.06.012.

[12] L. Tezza, M. Häusler, N. Conceição, M. I. Ferreira, Measuring and Modelling Soil Evaporation in an Irrigated Olive Orchard to Improve Water Management, Water 11 (2019) 2529. doi:10.3390/w11122529.

[13] G. Hasanain, T. Khallaf, K. Mahmood, Water evaporation from freshly placed concrete surfaces in hot weather, Cement and Concrete Research 19 (1989) 465–475. doi:10.1016/0008-8846(89)90035-5.

[14] K. Seifeddine, E. Toussaint, S. Amziane, Experimental Investigation on Evaporation Rate for Enhancing Evaporative Cooling of Pervious Pavement Containing Recycled Rubber, in: 4th International Conference on Bio-Based Building Materials, Barcelona, Spain, 2022, pp. 847–854. doi:10.4028/www.scientific.net/CTA.1.847.

[15] H. Hertz, Ueber die Verdunstung der Flüssigkeiten, insbesondere des Quecksilbers, im luftleeren Raume, Annalen der Physik 253 (1882) 177–193. doi:10.1002/andp.18822531002.

[16] V. P. Carey, Liquid-Vapor Phase-Change Phenomena: An Introduction to the Thermophysics of Vaporization and Condensation Processes in Heat Transfer Equipment, 2nd ed ed., Taylor and Francis, New York, 2008.

[17] Y. Akkus, A. T. Gurer, K. Bellur, Drifting mass accommodation coefficients: In situ measurements from a steady state molecular dynamics setup, Nanoscale and Microscale Thermophysical Engineering 25 (2020) 25–45. doi:10.1080/15567265.2020.1861139.

[18] K. Bellur, E. F. Médici, J. C. Hermanson, C. K. Choi, J. S. Allen, Modeling liquid–vapor phase change experiments: Cryogenic hydrogen and methane, Colloids and Surfaces A: Physicochemical and Engineering Aspects 675 (2023) 131932. doi:10.1016/j.colsurfa.2023.131932.

[19] K. Nabavian, L. Bromley, Condensation coefficient of water, Chemical Engineering Science 18 (1963) 651–660. doi:10.1016/0009-2509(63)85035-6.

[20] J. Barrett, C. Clement, Kinetic evaporation and condensation rates and their coefficients, Journal of Colloid and Interface Science 150 (1992) 352–364. doi:10.1016/0021-9797(92)90205-Z.

[21] L. D. Koffman, M. S. Plesset, L. Lees, Theory of evaporation and condensation, The Physics of Fluids 27 (1984) 876–880. doi:10.1063/1.864716.

[22] T. Ytrehus, S. Østmo, Kinetic theory approach to interphase processes, International Journal of Multiphase Flow 22 (1996) 133–155. doi:10.1016/0301-9322(95)00056-9.

[23] M. Knudsen, Die maximale Verdampfungsgeschwindigkeit des Quecksilbers, Annalen der Physik 352 (1915) 697–708. doi:10.1002/andp.19153521306.

[24] I. Eames, N. Marr, H. Sabir, The evaporation coefficient of water: A review, International Journal of Heat and Mass Transfer 40 (1997) 2963–2973. doi:10.1016/S0017-9310(96)00339-0.

[25] R. Marek, J. Straub, Analysis of the evaporation coefficient and the condensation coefficient of water, International Journal of Heat and Mass Transfer 44 (2001) 39–53. doi:10.1016/S0017-9310(00)00086-7.

[26] R. Schrage, A Theoretical Study of Interphase Mass Transfer, Ph.D. thesis, Columbia University Press, 1953.

[27] P. Wayner, Y. Kao, L. LaCroix, The interline heat-transfer coefficient of an evaporating wetting film, International Journal of Heat and Mass Transfer 19 (1976) 487–492. doi:10.1016/0017-9310(76)90161-7.

[28] P. C. Wayner, The effect of interfacial mass transport on flow in thin liquid films, Colloids and Surfaces 52 (1991) 71–84. doi:10.1016/0166-6622(91)80006-A.

[29] P. Davidovits, D. R. Worsnop, L. R. Williams, C. E. Kolb, M. Gershenzon, Comment on "Mass Accommodation Coefficient of Water: Molecular Dynamics Simulation and Revised Analysis of Droplet Train/Flow Reactor Experiment", The Journal of Physical Chemistry B 109 (2005) 14742–14746. doi:10.1021/jp0449915.

[30] R. Hołyst, M. Litniewski, D. Jakubczyk, M. Zientara, M. Woźniak, Nanoscale transport of energy and mass flux during evaporation of liquid droplets into inert gas: Computer simulations and experiments, Soft Matter 9 (2013) 7766. doi:10.1039/c3sm50997d.

[31] K. Bellur, E. F. Médici, C. K. Choi, J. C. Hermanson, J. S. Allen, Multiscale approach to model steady meniscus evaporation in a wetting fluid, Physical Review Fluids 5 (2020) 024001. doi:10.1103/PhysRevFluids.5.024001.

[32] M. Mozurkewich, Aerosol Growth and the Condensation Coefficient for Water: A Review, Aerosol Science and Technology 5 (1986) 223–236. doi:10.1080/02786828608959089.

[33] G. Barnes, The effects of monolayers on the evaporation of liquids, Advances in Colloid and Interface Science 25 (1986) 89–200. doi:10.1016/0001-8686(86)80004-5.

[34] G. wyllie, Evaporation and surface structure of liquids, Proceedings of the Royal Society of London. Series A. Mathematical and Physical Sciences 197 (1949) 383–395. doi:10.1098/rspa.1949.0071.

[35] E. M. Mortensen, H. Eyring, TRANSMISSION COEFFICIENTS FOR EVAPORATION AND CONDENSATION, The Journal of Physical Chemistry 64 (1960) 846–849. doi:10.1021/j100836a004.

[36] S. Fujikawa, M. Maerefat, A Study of the Molecular Mechanism of Vapour Condensation, JSME international journal. Ser. 2, Fluids engineering, heat transfer, power, combustion, thermophysical properties 33 (1990) 634–641. doi:10.1299/jsmeb1988.33.4_634.

[37] V. Badam, V. Kumar, F. Durst, K. Danov, Experimental and theoretical investigations on interfacial temperature jumps during evaporation, Experimental Thermal and Fluid Science 32 (2007) 276–292. doi:10.1016/j.expthermflusci.2007.04.006.

[38] A. Kryukov, V.Yu. Levashov, About evaporation–condensation coefficients on the vapor–liquid interface of high thermal conductivity matters, International Journal of Heat and Mass Transfer 54 (2011) 3042–3048. doi:10.1016/j.ijheatmasstransfer.2011.02.042.

[39] K. Montazeri, S. Hao, M. J. Abdolhosseini Qomi, Y. Won, Molecular Dynamics Investigation of Liquid and Vapor Interactions Near an Evaporating Interface: A Theoretical Genetics Perspective, Advanced Theory and Simulations 3 (2020) 2000017. doi:10.1002/adts.202000017.

[40] R. Meland, A. Frezzotti, T. Ytrehus, B. Hafskjold, Nonequilibrium molecular-dynamics simulation of net evaporation and net condensation, and evaluation of the gas-kinetic boundary condition at the interphase, Physics of Fluids 16 (2004) 223–243. doi:10.1063/1.1630797.

[41] T. Panczyk, Collisions of ideal gas molecules with a rough/fractal surface. A computational study, Journal of Computational Chemistry 28 (2007) 681–688. doi:10.1002/jcc.20472.

[42] H. K. Cammenga, H. Klinge, B. E. Rudolph, Untersuchungen über die Verdampfungs-Geschwindigkeit von Flüssigkeiten, Fortschrittsberichte über Kolloide und Polymere 55 (1971) 118–123. doi:10.1007/BF02826279.

[43] S. Takahama, L. M. Russell, A molecular dynamics study of water mass accommodation on condensed phase water coated by fatty acid monolayers, Journal of Geophysical Research 116 (2011) D02203. doi:10.1029/2010JD014842.

[44] D. E. Hagen, J. Schmitt, M. Trueblood, J. Carstens, D. R. White, D. J. Alofs, Condensation Coefficient Measurement for Water in the UMR Cloud Simulation Chamber, Journal of the Atmospheric Sciences 46 (1989) 803–816. doi:10.1175/1520-0469(1989)046<0803:CCMFWI>2.0.CO;2.

[45] J. F. Davies, R. E. H. Miles, A. E. Haddrell, J. P. Reid, Influence of organic films on the evaporation and condensation of water in aerosol, Proceedings of the National Academy of Sciences 110 (2013) 8807–8812. doi:10.1073/pnas.1305277110.

[46] K. J. Kossacki, J. Leliwa-Kopystynski, Temperature dependence of the sublimation rate of water ice: Influence of impurities, Icarus 233 (2014) 101–105. doi:10.1016/j.icarus.2014.01.025.

[47] A. Chatterjee, P. C. Wayner, J. L. Plawsky, D. F. Chao, R. J. Sicker, T. Lorik, L. Chestney, J. Eustace, R. Margie, J. Zoldak, The Constrained Vapor Bubble Fin Heat Pipe in Microgravity, Ind. Eng. Chem. Res. (2011) 10.

[48] A. Chatterjee, J. L. Plawsky, P. C. Wayner, D. F. Chao, R. J. Sicker, T. Lorik, L. Chestney, R. Margie, J. Eustace, J. Zoldak, Constrained Vapor Bubble Heat Pipe Experiment Aboard the International Space Station, Journal of Thermophysics and Heat Transfer 27 (2013) 309–319. doi:10.2514/1.T3792.

[49] A. Kundan, J. L. Plawsky, P. C.Wayner, Thermophysical characteristics of a wickless heat pipe in microgravity–constrained vapor bubble experiment, International Journal of Heat and Mass Transfer (2014) 1105–1113. doi:10.1016/j.ijheatmasstransfer.2014.07.044.

[50] A. Kundan, J. L. Plawsky, P. C. Wayner, Effect of Capillary and Marangoni Forces on Transport Phenomena in Microgravity, Langmuir 31 (2015) 5377–5386. doi:10.1021/acs.langmuir.5b00428.

[51] T. T. Nguyen, A. Kundan, P. C. Wayner, J. L. Plawsky, D. F. Chao, R. J. Sicker, Experimental study of the heated contact line region for a pure fluid and binary fluid mixture in microgravity, Journal of Colloid and Interface Science 488 (2017) 48–60. doi:10.1016/j.jcis.2016.10.082.

[52] J. Plawsky, Constrained Vapor Bubble Experiment (CVB) in the Light Microscopy Module (LMM), Gravitational and Space Research 12 (2024) 60–63. doi:10.2478/gsr-2024-0004.

[53] C. Payne, Physical Sciences Informatics (PSI), http://www.nasa.gov/PSI, 2020.

[54] J. L. Plawsky, P. C. Wayner, Explosive nucleation in microgravity: The Constrained Vapor Bubble experiment, International Journal of Heat and Mass Transfer 55 (2012) 6473–6484. doi:10.1016/j.ijheatmasstransfer.2012.06.047.

[55] P. Linstrom, NIST Chemistry WebBook, NIST Standard Reference Database 69, 1997. doi:10.18434/T4D303.

[56] G. Nagayama, T. Tsuruta, A general expression for the condensation coefficient based on transition state theory and molecular dynamics simulation, Journal of Chemical Physics 118 (2003) 1392–1399. doi:10.1063/1.1528192.

[57] A. Kundan, T. T. T. Nguyen, J. L. Plawsky, P. C. Wayner, D. F. Chao, R. J. Sicker, Condensation on Highly Superheated Surfaces: Unstable Thin Films in a Wickless Heat Pipe, Physical Review Letters 118 (2017) 094501. doi:10.1103/PhysRevLett.118.094501.